3-2009

Blue-shifted Emission in CdTe/ZnSe Heterostructured Nanocrystals

Nishshanka N. Hewa-Kasakarage

Nilanka P. Gurusinghe

Mikhail Zamkov
Bowling Green State University, zamkovm@bgsu.edu

Blue-Shifted Emission in CdTe/ZnSe Heterostructured Nanocrystals

Nishshanka N. Hewa-Kasakarage, Nilanka P. Gurusinghe, and Mikhail Zamkov*

The Center for Photochemical Sciences and Department of Physics, Bowling Green State University, Bowling Green, Ohio 43403

Received: December 4, 2008; Revised Manuscript Received: January 12, 2009

Properties of colloidal heterostructured nanocrystals are largely determined by the spatial distribution of photogenerated carriers across the junction of semiconductor materials that form the heterostructure. The two known types of carrier distributions are identified based on whether both carriers reside within the same (type I) or opposite (type II) sides of the heterojunction. Here we demonstrate the existence of another type of spatial carrier distribution in heteronanocrystals, which corresponds to the localization of both charges along the material junction. Such localization pattern was realized in novel CdTe/ZnSe heteronanocrystals, where the expected type I infrared emission was dominated by more intense photoluminescence in the 570−600 nm range, corresponding to the recombination of carriers within an interfacial alloy layer, formed by the cation and anion exchange between CdTe and ZnSe phases. Fabricated heteronanocrystals exhibit excellent optical characteristics including near-single-exponential lifetimes, enhanced emission stability, and fluorescence emission quantum yields of up to 24%.

1. Introduction

Conjoining different semiconductor nanostructures in a single quantum dot (QD) provides synthetic means for the development of novel optoelectronic materials. Indeed, through an appropriate selection of their nanoscale components, such heteronanocrystals (NCs) offer a superior control over the spatial distribution of carriers across material interfaces, which determines an overall functionality of the quantum system. Conventionally, a heterojunction of the two semiconductor materials can be classified as either type I, where both carriers are confined within the same semiconductor, or type II, where an electron and a hole are spatially separated in two different parts of the heterostructure. Because of the highly stable emission of NCs in the first group,[1−3] their properties are readily utilized in applications that require coupling of a QD to organic moieties, such as in hybrid light-emitting diodes (LEDs)[4−6] or in vivo imaging,[7,8] where the use of a binary QDs can lead to an irreversible loss of fluorescence,[9,10] or severe blinking.[11−13] Heterostructures of the second group, on the other hand, benefit from an efficient separation of charges between the core an the shell, which makes them useful in photovoltaic applications,[14−18] where spatial charge separation reduces an exciton dissociation potential, or QD-based lasers,[19−21] where an electric dipole of a photogenerated pair Stark-shifts the biexciton level resulting in a desirable linear light amplification regime.

One common feature, characteristic to above-mentioned carrier localization types is a straightforward correspondence between a QD emission range and the energy spacing between the two closest band edges of semiconductor materials that form a heterostructure. Indeed, for both type I and type II hetero-NCs, the energy of emitted photons is determined by the energy difference between the closest zero-angular momentum states, 1S(e) and $1S_{3/2}$(h), of the adjoined materials.

Here we show that II−VI semiconductor hetero-NCs can also emit in a wavelength range that does not correspond to any of the electronic transitions that can be expected from the band structure of their core- or shell-located materials, such that localization of carriers in these structures can no longer be classified as type I or type II. This behavior was demonstrated in novel CdTe/ZnSe core/shell hetero-NCs fabricated via organometallic routes. In addition to a weak infrared fluorescence that was expected due to a type I band alignment in a CdTe/ZnSe NC arrangement, we observed a blue-shifted emission peak, with associated quantum yield (QY) of up to 24%. Present study shows that emission in CdTe/ZnSe hetero-NCs arises from the recombination of carriers within an interfacial layer, which is formed along the core/shell interface due to the interdiffusion of Se and Zn ions into CdTe lattice during shell deposition. This type of electron−hole localization has been previously observed in CdTe/ZnSe quantum wells, where atomic interdiffusion at the junction of the two semiconductor thin films lead to the formation of an alloy layer emitting in the 520−600-nm range.[22,23]

Besides answering related fundamental questions, the demonstrated emission in CdTe/ZnSe hetero-NCs could be of interest to a number of applications, including the development of sensors utilizing Förster resonance energy transfer (FRET),[24,25] where interfacial localization of excitons can help reducing an effective distance between donor and acceptor moieties. Biological sensor applications of CdTe/ZnSe materials should also benefit from the fact that only a few monolayers (MLs) of ZnSe shell efficiently decouple electronic wave functions in CdTe/ZnSe hetero-NCs from the surface environment, which permits a simultaneous realization of the near-surface excitations and improved emission stability.

2. Experimental Section

2.1. Chemicals. Cadmium oxide (99%, Aldrich), Se powder (99.5%, Aldrich), Te powder (99.99%, Aldrich), 1-octadecene (ODE, 90%, Aldrich) tributylphosphine (TBP, 99%, Aldrich), oleic acid (OA, 90%, Aldrich), trioctylphosphine (TOP, 97%, Strem), trioctylphosphine oxide (TOPO, 99%, Aldrich), hexadecylamine (HDA, 99%, Aldrich), $ZnEt_2$ (97% pure, 10% by

* To whom correspondence should be addressed. E-mail: zamkovm@bgsu.edu.

10.1021/jp8106843 CCC: $40.75
Published on Web 02/23/2009

weight in hexane, Strem), benzoyl peroxide (BPO, 97%, Aldrich), benzylamine ($BzNH_2$, 99%, Acros), anhydrous hexane (Aldrich), methanol (Aldrich), chloroform (Acros), and toluene (Aldrich) were used as purchased.

2.2. Synthesis of CDTe Nanocrystals. All reactions were conducted under argon atmosphere using standard Schlenk techniques. Synthesis of monodisperse zinc blende CdTe nanocrystals was based on the procedure described previously.[26] Namely, 0.0128 g (0.1 mmol) of cadmium oxide was dissolved in 0.2 mL (0.63 mmol) of oleic acid and 4.9 mL (3.87 g) of ODE by heating reagents to 280 °C in the 25-mL three-neck flask while stirring. After the mixture became clear, tellurium stock solution, prepared by dissolving 0.0064 g (0.05 mmol) of tellurium in 0.07 mL of TBP and 1.25 mL (0.986 g) of ODE was swiftly injected into the reaction flask. During the nanocrystal growth, the temperature was kept at 270 °C. The reaction was stopped after 0.5−5 min, depending on the desired nanocrystal size, by removing the flask from the heating mantle.

2.3. Purification of CdTe Nanocrystals. After the reaction mixture was allowed to cool down to 50 °C, 3−5 mL of hexane was added into the solution to prevent solidification. The subsequent cleaning of nanocrystals was done by hexane/methanol extraction. Typically 6−7 mL of methanol was slowly added to the reaction mixture in hexane, which was then centrifuged for 10 min at 3500 rpm. The upper hexane layer containing CdTe NCs was taken with a syringe for further purification. Eventually a clear solution of nanoparticles in hexane was obtained. The suspension was then placed under argon and stored in the dark for future shell deposition.

2.4. Overcoating with ZnSe. A mixture of 1.7 g (4.4 mmol) of TOPO and 1.5 g (6.6 mmol) of HDA in a 25-mL three-neck flask was degassed at 140 °C for 1 h under vacuum. The solution was then allowed to cool down and transferred to argon gas. At this stage, 1.8 mL (1.5 g) of TOP and all of prepared previously CdTe nanocrystals were added to the flask and heated to 240 °C. Se solution was prepared by dissolving 0.032 g (0.4 mmol) of Se powder in 1.8 mL (1.5 g) of TOP. Zn injection solution was prepared by mixing 1.5 mL of 10% diethylzinc with 1.8 mL (1.5 g) of TOP and heating the mixture to 75 °C for 2 h while stirring in order to form TOP-Zn complexes. During the overcoating procedure a mixture of Zn/Se stock solutions was injected into the reaction flask with CdTe NCs at 240 °C at a rate of 0.015 mL per minute. Aliquots of the growth solution were taken at 5-min intervals for UV−vis and photoluminescence (PL) spectral characterization. The reaction was stopped in approximately 40 min, and the mixture was cooled down to 70 °C. For shell deposition via successive ion layer adsorption reaction (SILAR), 0.1 mL injections of Zn and Se stock solutions were made sequentially every 5−8 min starting with Zn ions. The total of 5 monolayers were grown.

2.5. Synthesis of Ternary ($Cd_xTe_yZn_{1-x}$, $Cd_yTe_xSe_{1-x}$, $Zn_yTe_xSe_{1-x}$) and Quarternary ($Zn_xCd_{1-x}Se_yTe_{1-y}$) Nanocrystals. A unified approach to synthesis of ternary and quarternary alloy nanocrystals was based on procedures adapted from previous studies.[27−29] In the first step, CdO was decomposed in the reaction flask by dissolving 0.0128 g (0.1 mmol) of cadmium oxide in 0.2 mL (0.63 mmol) of oleic acid and 4.9 mL (3.87 g) of ODE at 260−290 °C. In separate vials, tellurium, zinc, and selenium stock solutions were made by dissolving 0.05 mmol of the corresponding source (Te powder, diethylzinc, Se powder, respectively) in 1.8 mL of TOP. During synthesis of alloy nanocrystals, appropriate stock solutions were combined and injected into the reaction flask at 260 °C. The injection rate was 0.02 mL per minute.

2.6. Etching with BPO. Controlled etching of nanocrystals with BPO was done following the technique described previously.[30,31] Prior to etching of nanocrystals with BPO their surface ligands were exchanged to a shorter benzylamine by placing 0.5 mL of purified CdTe/ZnSe NCs in hexane of a concentration in about 2 mL of benzylamine. The mixture was then sonicated for approximately 15−20 min or until the nanocrystals were totally dispersed yielding a clear solution. 1.0 mL of this suspension was added to 5.0 mL of a 3:1 toluene/methanol mixture. To initiate the etching process, a solution of benzoyl peroxide (0.165 M in 1:1 toluene/methanol) was quickly injected into the nanocrystal suspension. The etching process was monitored using a home-built confocal microscope fiber-coupled to a spectrometer.

2.7. Characterization. UV−vis absorption and PL spectra were recorded using a CARY 50 scan spectrophotometer and Jobin Yvon Fluorolog FL3−11 fluorescence spectrophotometer. PL quantum yield of CdTe/ZnSe nanocrystals was determined relative to known QYs of several organic dyes excited at 400−440 nm. High resolution transmission electron microscopy measurements were carried out using JEOL 311UHR operated at 300 kV. Specimens were prepared by depositing a drop of nanocrystal hexane solution onto a Formvar-coated copper grid and letting it dry in air. X-ray powder diffraction measurements were carried out on Scintag XDS-2000 X-Ray Powder Diffractometer. Picosecond transient absorption (TA) technique utilized a Ti: Sapphire regenerative amplifier TOPAS-C combination and operated at 1 kHz. Instrument response time was estimated to be less than 1 ps. Further details about the TA system can be found in a previous work.[32]

2.8. Fluorescence Lifetime Measurements. Fluorescence lifetime measurements were performed using a time correlated single photon counting setup utilizing SPC-630 single photon counting PCI card (Becker & Hickle CmbH), with a picosecond diode laser operating at 400 nm as an excitation source (Picoquant), and id50 avalanche photodiode (Quantique). The repletion rate of the laser was chosen to allow for a 360 nm time window, and the pulse fluence was adjusted to produce about 1 emission photon per 100 excitation pulses.

3. Results and Discussion

The energy diagram of zero-angular momentum states in a CdTe/ZnSe core/shell system, estimated from known NC sizes and bulk band gap values for CdTe and ZnSe materials,[33] is shown Figure 1. Both conduction and valence band edges of CdTe are located within the energy gap of ZnSe, which is consistent with the type I localization regime, where an excited electron−hole pair resides primarily in the core of the heterostructure. The corresponding transition energy for such spatial arrangement of charges is expected to be somewhat lower than the transition energy of binary CdTe NCs due to the increased delocalization of carriers caused by tunneling of electronic wave functions into the ZnSe layer.[34] Contrary to these expectations, the observed emission in CdTe/ZnSe hetero-NCs is shifted toward higher energies with respect to the position of the FL peak in CdTe, as shown in Figure 1b. This is an unusual result, since recombination of $1S(e)$-$1S_{3/2}(h)$ carriers in either type I or type II structure should not result in photon energies that exceed the band gap values of the either the core or the shell material. Consequently, blue-shifting of the emission upon the deposition of ZnSe shell indicates that the heterojunction in CdTe/ZnSe hetero-NCs is likely to have a more complex composition than that of conventional core/shell NCs.

The shape and size distribution of CdTe/ZnSe hetero-NCs were analyzed using transmission electron microscopy (TEM).

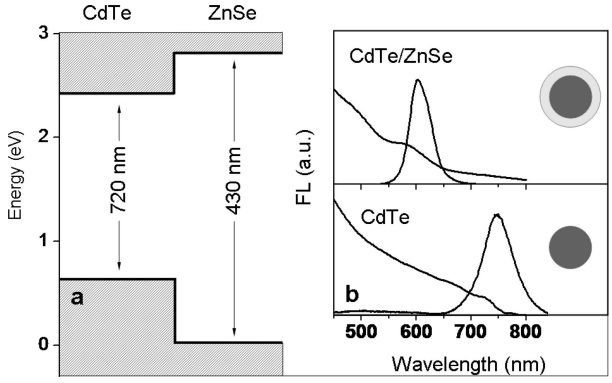

Figure 1. (a) Energy diagram showing a type I band edge alignment in CdTe/ZnSe core/shell NCs. (b) Spectral analysis of nanocrystal emission. The position of the FL peak in CdTe/ZnSe hetero-NCs is blue-shifted with respect to the emission of CdTe NC cores, which does not correspond to type I carrier confinement expected from the energy diagram in part a.

Figure 2a shows the structure of CdTe NCs prior to the deposition of ZnSe shell. Most NCs appear to have a tetrapodlike shape with an average size of 7 nm (see Figure 2b), which is calculated by measuring the length of one of its branches (extensions). The mean width of tetrapod branches as well as the average diameter of the central apex were found to be 50−60% of the extension length. The subsequent growth of ZnSe shell resulted in a 2-nm increase in the average length of the structure, as evident from the comparison of size distributions for CdTe and CdTe/ZnSe nanoparticles in parts b and c of Figure 2. The deposition of ZnSe also lead to the increase in the average width of the tetrapod branch (6−7 nm) as well as the standard deviation of the length distribution from 7 to 11%.

Changes in the crystal structure and composition of CdTe NCs caused by the deposition of ZnSe shell were investigated using a combination of X-ray powder diffraction (XPD) and energy dispersive X-ray (EDX) techniques. The experimental diffraction pattern of the original CdTe NCs is shown in Figure 3c, where the three main peaks corresponding to the cubic phase of bulk CdTe lattice are clearly identified. CdTe/ZnSe hetero-NCs, prepared by depositing a maximum of 2−3 ML of ZnSe (as calculated from the amount of Zn and Se elements in injection solutions), exhibit a second set of Bragg peaks that are shifted toward higher diffraction angles with respect to those in CdTe (see Figure 3b), as expected due to a smaller lattice spacing in ZnSe. The profile of the observed Bragg peaks in CdTe/ZnSe hetero-NCs, however, appears to be unusually broad. Despite a substantial difference in lattice constants of CdTe and ZnSe semiconductor materials, their individual phases cannot be resolved in the experimental pattern, indicating a possible formation of a ternary alloy composition, similar to CdSe crystal phase (Figure 3e) that contributes to the diffraction signal at intermediate angles and leads to inhomogeneous broadening of Bragg peaks. This transitional crystal structure is likely to take up a sizable portion of synthesized nanoparticles, as can be inferred from near-equal XPD intensities corresponding to diffraction angles of binary CdTe, CdSe, and ZnSe, as well as intermediate ternary alloy structures. Additional experimental evidence supporting the existence of a crystalline phase different from that of CdTe and ZnSe materials is provided by EDX analysis of the elemental composition, shown in Figure 3a. The molar ratio of elements derived from the raw X-ray count, Cd:Se:Zn:Te = 1:0.68:0.46:0.35, indicates that the amount of Cd in fabricated materials could be in excess of either chalcogen, which is consistent with the simultaneous formation of both Cd−Se and Cd−Te crystalline bonds.

The growth kinetics of the reaction mixture is summarized in Figure 4a, where the evolution of fluorescence and absorption spectra is shown for different stages of ZnSe shell deposition. Upon the initial injection of Zn and Se precursors into the reaction flask, emission intensity of the original CdTe NCs (bottom panel) subsides, while a new FL feature appears at 565 nm. During the subsequent shell growth, this high-energy peak gradually red-shifts, reaching the saturation value of 595−600 nm. The nanoparticle growth is also accompanied by a steady increase in the quantum yield, which, for as-prepared samples in chloroform, was approaching 24%. Changes in the absorption spectrum of CdTe NCs, associated with the deposition of the ZnSe shell, are investigated in Figure 4b. The first injection of Zn and Se precursors into the growth solution red-shifts the absorption edge in CdTe NCs (blue arrow) leading to the formation of a monotonous tail, which extends into an infrared region. The increase in absorption at energies below the CdTe band gap (green arrow 3) is likely the result of a type I delocalization of $1S(e)1S_{3/2}(h)$ excitons in CdTe cores, caused by tunneling of excited carriers into an interfacial layer or ZnSe shell (see Supporting Information for details). It appears that while most excitations in CdTe/ZnSe hetero-NCs recombine through a 600-nm decay channel, a small portion of excitons lacks a sufficient energy to undergo such transition and can channel through a low-energy band gap of CdTe cores. This leads to broadening of the absorption edge near 725 nm and produces a weak infrared emission, which is shown in Figure 4c (green arrow), along with the main emission peak at 600 nm. Red-shifting of such residual emission in CdTe NCs (green arrow) upon shell deposition provides additional support to the fact that the decrease in the absorption energy of CdTe NCs (Figure 4b, blue arrow) is caused by tunneling of $1S(e)1S_{3/2}(h)$ excitons into a wider band gap layer surrounding the core.

As expected from XPD measurements that indicate the existence of at least three distinct crystalline phases, absorption profile of CdTe/ZnSe hetero-NCs contains three separate peaks, denoted as 1, 2, and 3 in Figure 4b, which, in view of the above discussion, were attributed to $1S(e)$-$1S_{3/2}(h)$ transitions in ZnSe, interfacial layer, and CdTe materials, respectively. Such arrangement, however, poses a nonconforming issue concerning a long-lived localization of carriers within the interfacial layer, as manifested by a strong emission around 600 nm. Indeed, since the band gap of the interfacial crystalline phase is wider than that of CdTe, at least one of the carriers should be transferred into the core material promptly upon excitation. This should result in strengthening of the infrared emission at 780−800 nm, which, in present experiments, however, is relatively weak.

To understand the temporal dynamics of carrier relaxation in CdTe/ZnSe hetero-NCs we have employed the time-resolved picosecond transient absorption (TA) technique, which allows measuring the excited states population ratios (state filling factors) in real time. Bleaching of the lowest in energy absorption feature (1S) in NCs occurs primarily as a result of the photoexcited electrons residing in 1S(e) state.[35] The contribution of holes to the bleach is insignificant because the valence band state involved in the absorbing transition remains unoccupied until the lower-energy emitting hole state is completely filled, which only occurs at high excitation levels.[36] The contribution of holes to 1S bleach is further reduced due to high spectral density of valence states, which results in the spread of hole populations across many adjacent states, not all

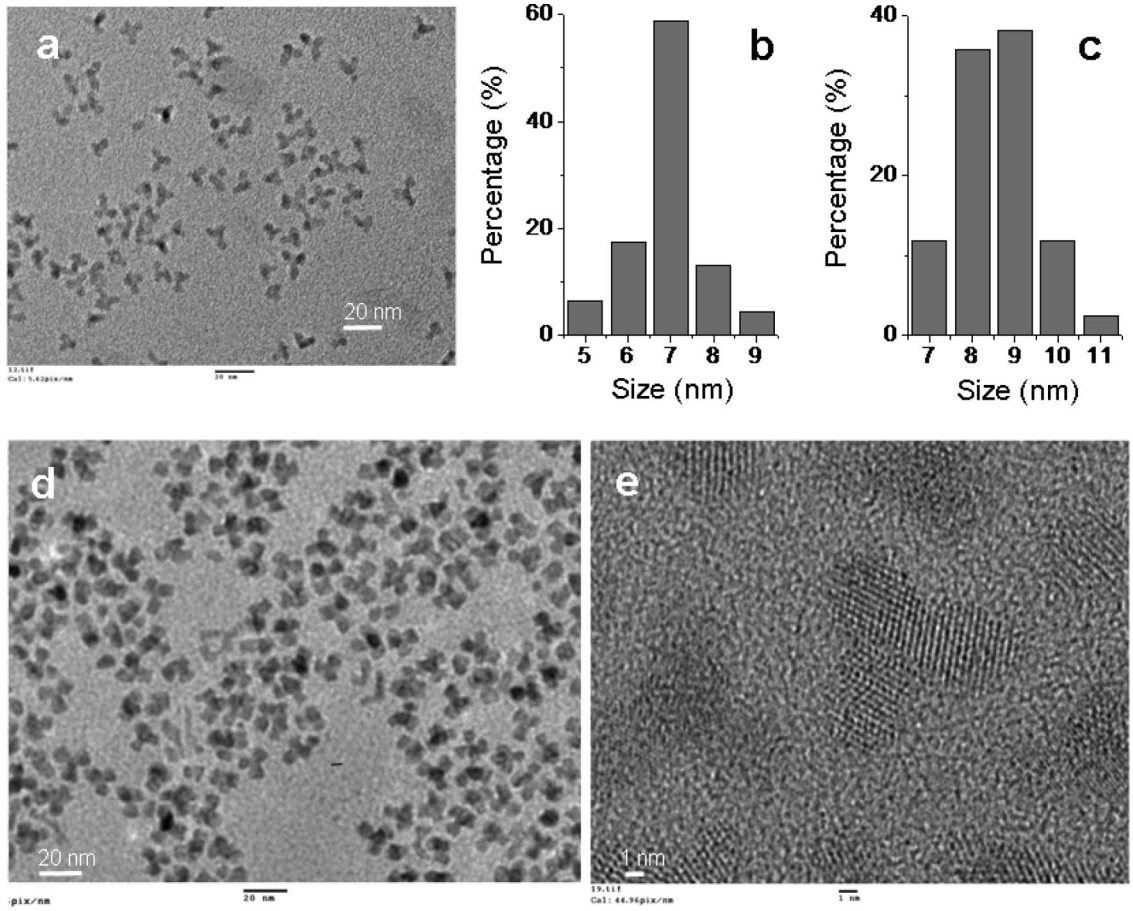

Figure 2. (a) High-resolution TEM images of CdTe NCs. (b and c) Statistical distributions of lengths for tetrapod-shaped CdTe and CdTe/ZnSe NCs, respectively. (d) High-resolution TEM images of CdTe/ZnSe hetero-NCs (e) High-magnification images of CdTe/ZnSe hetero-NCs showing the lattice structure. Scale bars are (a) 20 nm, (d) 20 nm, and (e) 1 nm.

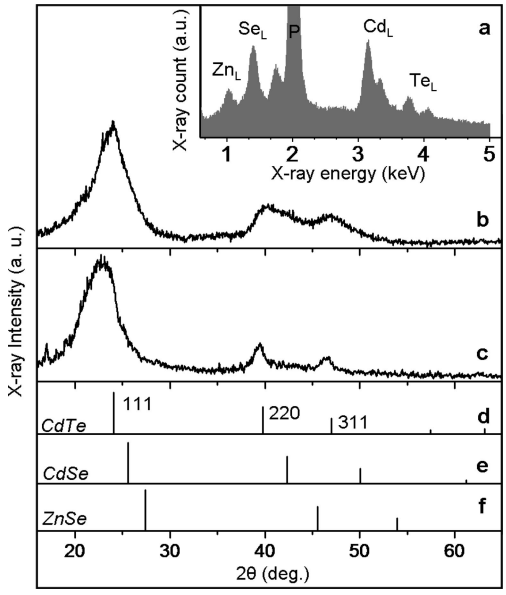

Figure 3. XPD and EDX analysis of CdTe/ZnSe hetero-NCs (a) EDX spectrum of CdTe/ZnSe hetero-NCs, obtained at 20 keV. XPD spectra of CdTe/ZnSe (b) and CdTe (c) NCs along with diffraction patterns of bulk cubic CdTe (d), CdSe (e), and ZnSe (f).

of which are optically coupled to 1S(e). This also reduces the contribution of the stimulation emission into the TA signal.

Figure 5c shows the time dependence of absorbance changes in CdTe/ZnSe hetero-NCs, excited with 420-nm monochromatic light. The spectrum contains two main areas of bleaching, corresponding to spectral markers at 470 and 595 nm. By comparison of observed bleach positions with the absorption spectrum in Figure 4b, we were able to classify the origin of bleaching signals at 470 and 595 nm as due to $1S(e)-1S_{3/2}(h)$ transitions in ZnSe shell and CdTe/ZnSe interfacial layer, respectively. Both 470- and 595-nm bands are quickly bleached upon excitation due to the injection of carriers into corresponding electronic states. The excited carrier population then undergoes the initial fast recovery via nonradiative processes, which is followed by a slower radiative decay. Changes in the absorption of the 595-nm band at negative times, associated with the emission of hetero-NCs, are sufficiently slow in comparison with nonradiative processes and do not alter the observed relaxation trend. Figure 5b shows two decay traces that correspond to the temporal bleach recovery for 470- and 595-nm excitations. At early times, changes in the absorption of 470-nm band occur at a faster rate than those of the 595-nm band, indicating a more robust migration of carriers through nonradiative channels in ZnSe material. While the observed behavior could simply indicate the difference in nonradiative decay rates associated with 470-nm and 595-nm bands, it might also be the result of a correlation between the two excitations. More specifically, transfer of carriers from excited states in ZnSe shell to unoccupied potential minimum states in CdTe/ZnSe hetero-NCs is allowed energetically and could explain the observed difference in the initial fast bleach recovery.

PLE scan, shown in Figure 5a, provides further evidence supporting the migration of excited carriers from ZnSe shell into the interfacial layer of CdTe/ZnSe hetero-NCs. In these

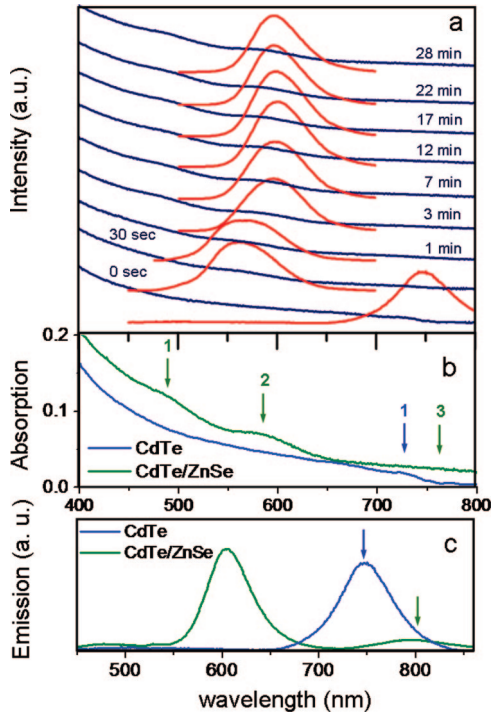

Figure 4. (a) Changes in the UV−vis absorption and room-temperature fluorescence spectra of CdTe and CdTe/ZnSe hetero-NCs during shell deposition. The bottom panel corresponds to the original CdTe core NCs, while top panels show the temporal evolution of spectral features of the growth solution. (b) Comparison of the absorption spectra of CdTe (blue) and CdTe/ZnSe (green) NCs. An absorption edge in CdTe NCs, located near 725 nm (blue arrow) is red-shifted upon deposition of ZnSe shell, giving rise to a monotonous tail, which extends into the infrared region. This process is accompanied by the appearance of the two peaks at higher energies, corresponding to a band gap absorption in ZnSe (green arrow 1) and the absorption of interdiffusion layer states (green arrow 2). (c) Changes in the emission of CdTe NCs (blue curve) produced by the deposition of a thin ZnSe layer. In addition to the primary peak at 600 nm, the emission spectrum of CdTe/ZnSe hetero-NCs contains the residual emission in CdTe cores (green arrow), which is red-shifted with respect to the position of the FL peak in binary CdTe NCs.

measurements, the detection wavelength was set at the primary emission maximum, and the excitation source was tuned from 400 to 600 nm. The observed PLE profile exhibits two emission maxima corresponding to excitation wavelengths of 470 and 595 nm attributed to $1S(e)$-$1S_{3/2}(h)$ transitions in ZnSe shell and the interfacial layer, respectively. The observed contribution of the 470-nm absorption peak into the PLE emission at 600 nm is consistent with the proposed picosecond transfer of excitations from the shell into the interfacial layer.

One possible mechanism for the formation of the proposed interfacial layer in CdTe/ZnSe hetero-NCs is via replacement of Te ions in CdTe NCs with Se, whereby creating an intermediate alloy on which the now better lattice-matched ZnSe can subsequently grow. Cd to Zn cation exchange is another possibility that may lead to a blue-shifted emission in CdTe/ZnSe hetero-NCs. To test these hypotheses, we have looked for similarities between optical properties of fabricated CdTe/ZnSe hetero-NCs and several alloy nanoparticles, which composition may resemble the interfacial layer, including ternary ($Cd_xTe_yZn_{1-x}$, $Cd_yTe_xSe_{1-x}$, $Zn_yTe_xSe_{1-x}$) and quaternary ($Zn_xCd_{1-x}Se_yTe_{1-y}$) NCs. While the final stoichiometric ratios of elements in fabricated alloy NCs cannot be determined precisely, our main focus is in learning about emission properties of nanoparticles that grow when certain elements, in proportions similar to those used for CdTe/ZnSe hetero-NCs synthesis, are allowed to react. First, $Cd_xTe_yZn_{1-x}$ alloy NCs were fabricated by simultaneous injection of Te and Zn precursors into a hot reaction mixture containing Cd solution in oleic acid/ODE. The formation of the small amount of binary ZnTe and CdTe NCs in the reaction flask was confirmed by FL peaks at 480 and 690 nm, as shown by a green curve in Figure 6a. The emission corresponding to the ternary crystalline phase, the presence of which was verified by XPD measurements, however, could not be distinguished in the emission spectra. Similar trend was also observed for $Zn_yTe_xSe_{1-x}$ NCs, where optical spectra contained characteristic FL peaks of binary QDs but showed no indication of alloy nanoparticles, possibly due to the intrinsically low QY for a ternary phase. A somewhat stronger FL signal corresponding to the ternary alloy structure was observed for $Cd_yTe_xSe_{1-x}$ NCs, along with the less prominent CdSe binary peak, as shown by a blue curve in Figure 6a. The position of the FL peak was found to be at 720 nm, which is outside the range of emission of CdTe and CdSe NCs, as expected due to a significant optical bowing[37] in $Cd_yTe_xSe_{1-x}$ alloys. This effect is known to reduce the energy of the ternary band gap below the corresponding binary values such that $E_g(CdSe_xTe_{1-x}) = xE_g(CdSe) + (1-x)E_g(CdTe) - bx(1-x)$. Finally, we have attempted the synthesis of quaternary alloy NCs by combining all three precursors, Zn, Te, and Se, with the Cd solution in the reaction flask. The emission spectrum of the resulting nanoparticle suspension (see the red curve in Figure 6a) in hexane shows high-intensity FL peak near 600 nm, along with low intensity peaks corresponding to binary NCs.

On the basis of the observed emission ranges of ternary and quaternary NCs as well as the results of TA, PLE, EDX, XPD, PL, and steady-state absorption measurements, we propose that the interfacial layer in fabricated hetero-NCs has a gradient composition such that the inner CdTe core is overcoated with a strongly emissive $Zn_xCd_{1-x}Se_yTe_{1-y}$ alloy, formed via Se/Te and Zn/Cd exchange, followed by a ZnSe shell layer. This idea is illustrated in Figure 6b. The presence of CdTe material within CdTe/ZnSe hetero-NCs has been confirmed by XPD, FL, and steady-state absorption measurement, while the presence of ZnSe shell is supported by XPD, absorption, TA, and PLE techniques. Formation of the CdSe-like $Zn_xCd_{1-x}Se_yTe_{1-y}$ emissive layer ($x \ll y < 1$) is consistent with broadening of the (220) and (311) Bragg peaks in XPD spectra, which is caused by the development of an intermediate lattice spacing. Such quaternary interfacial composition can also explain an excessive amount of Cd and Se elements in CdTe/ZnSe hetero-NCs observed in EDX measurements. Finally, CdSe-rich $Zn_xCd_{1-x}Se_yTe_{1-y}$ alloy appears to be the only composition with an intermediate lattice spacing that produces a strong emission in the 600-nm range.

Within the proposed scheme, photogenerated electrons are believed to be localized at the interface of CdTe and ZnSe materials, where the energy of CdSe-like conduction band edge dips lower than the corresponding levels in CdTe and ZnSe NCs (Figure 6b). Meanwhile, highest in energy hole states are located in CdTe cores, which should favor the $1S_e(Zn_xCd_{1-x}Se_yTe_{1-y})$-$1S_h(CdTe)$ carrier relaxation pathway, yet the radiative decay of carriers is observed through both CdTe and $Zn_xCd_{1-x}Se_yTe_{1-y}$ hole states. This can be attributed to the existence of two competing decay channels that exhibit very little hole exchange. The reason for such hole confinement within $Zn_xCd_{1-x}Se_yTe_{1-y}$ layer is difficult to determine in the present study due to a lack of information on the precise interfacial stoichiometry and could be interesting to explore in the future work.

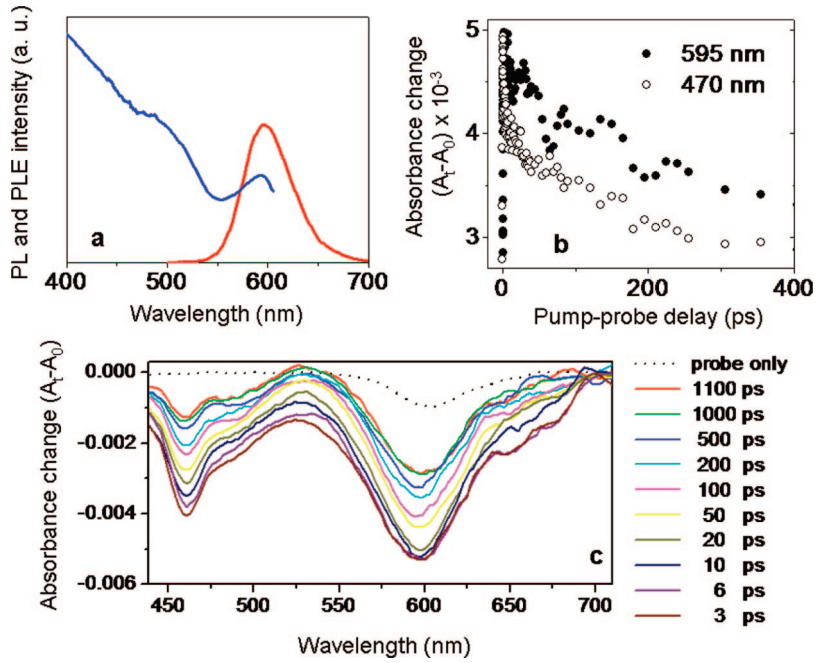

Figure 5. (a) PL and PL excitation (PLE) spectra of CdTe/ZnSe hetero-NCs. The detection wavelength was set at the primary emission maximum, and the excitation source was tuned from 400 to 600 nm. (b) Bleach recovery (inverted) of the two primary absorption bands in CdTe/ZnSe hetero-NCs associated with 1S(e)-1$S_{3/2}$(h) transitions in ZnSe shell and the interfacial alloy, respectively. (c) Temporal evolution of absorbance changes in CdTe/ZnSe hetero-NCs, calculated by taking the difference of absorption spectra before and after the excitation pulse. The dotted line represents the contribution from NC emission.

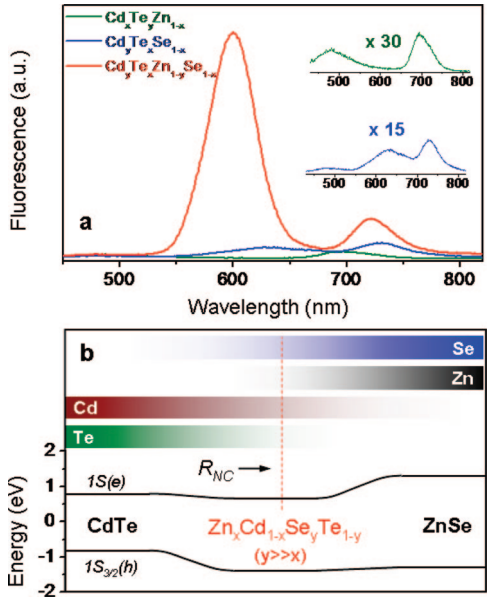

Figure 6. (a) Emission spectra of ternary $Cd_xTe_yZn_{1-x}$ (green curve), $Cd_yTe_xSe_{1-x}$ (blue curve), and quaternary $Zn_xCd_{1-x}Se_yTe_{1-y}$ (red curve) alloy nanocrystals. The strongest emission is observed in quaternary NCs, which composition is believed to be the closest to the composition of the emissive interfacial layer in CdTe/ZnSe hetero-NCs. (b) Proposed radial dependence of 1S(e) and 1$S_{3/2}$(h) state energies in CdTe/ZnSe hetero-NCs.

Fluorescence lifetime measurements can provide a viable tool for distinguishing between different types of excitations that exist in a quantum system. From this prospective, excitons that are localized at the interface of CdTe/ZnSe hetero-NCs represent a unique class of electronic excitations, the recombination mechanism of which is intrinsically different from that of volumetric excitons in CdTe NCs. As a result, the FL lifetime of the 600-nm emission peak should be distinguishable from the lifetime of the band-edge FL in CdTe NCs. To test this

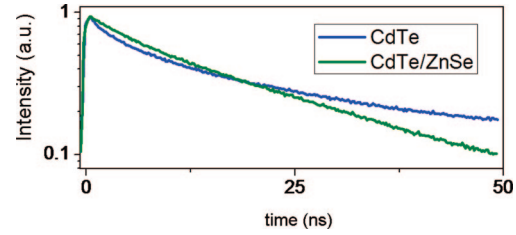

Figure 7. FL decay traces for CdTe (blue) and CdTe/ZnSe (green) NCs, measured by means of the time-correlated single photon counting technique.

hypothesis, we have measured decay traces of CdTe and CdTe/ZnSe NCs using the standard time-correlated single photon counting technique.

Figure 7 shows temporal changes in the intensity of the FL emission for these nanostructures. Significant differences can be seen both in the character and the lifetime of the observed decay curves. CdTe core NCs (blue curve) exhibit a nonexponential relaxation of fluorescence, which is generally expected for semiconductor QDs.[38] The FL decay of CdTe/ZnSe hetero-NCs (green curve), on the other hand, is nearly single-exponential ($R^2 = 0.997$), which demonstrates a unique character of optical excitations in CdTe/ZnSe hetero-NCs. Indeed, a simple addition of a wide-band gap semiconductor shell onto a CdTe core should result in a minor increase in the FL lifetime without a significant change in the decay character. Contrary to these expectations the deposition of a ZnSe shell causes dramatic changes in the relaxation character and leads to slightly shorter decay times. Both of these changes are consistent with an increased carrier confinement in CdTe/ZnSe hetero-NCs corresponding to interfacial character of these excitations.

The ZnSe shell in CdTe/ZnSe hetero-NCs serves as a barrier, which separates electronic excitations at the core/shell interface from nanocrystal surroundings. The resulting structure, therefore, is self-passivating, and its optical properties are expected to be less susceptible to the surface environment than those of binary

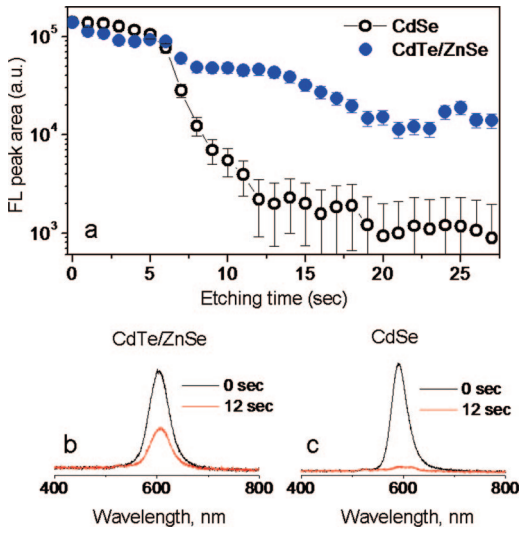

Figure 8. (a) Comparison of FL quenching kinetics during etching with BPO for CdSe and CdTe/ZnSe NCs. FL spectra of CdTe/ZnSe (b) and CdSe (c) NCs prior to etching (black curve) and after 12 s of etching (red curve).

QDs. Given the CdSe-like composition of the emissive layer in fabricated CdTe/ZnSe hetero-NCs their emission stability is evaluated in comparison with that of CdSe NCs. Such measurements can provide additional proof that the outside layer of wide-band gap ZnSe material is, in fact, present in fabricated structures. The effect of surface environment is introduced via a mild etching with BPO, which allows for a controlled removal of outer layers from nanocrystals. This approach simulates the contamination of the NC lattice with ions and structural defects that typically lead to the irreversible loss of band gap fluorescence due to carrier trapping. Figure 8 shows the kinetics of FL quenching during the etching process for both CdTe/ZnSe and CdSe suspensions with equal concentrations of nanoparticles in hexane. As seen by the reaction traces, emission of CdSe NCs becomes fully quenched within 10−12 s following the addition of BPO, while the emission of CdTe/ZnSe hetero-NCs is reduced only by 50% over the same time period. Similar trend has been consistently observed in subsequent measurements utilizing different concentrations of BPO and longer etching times, which indicates an overall greater stability of CdTe/ZnSe emission in comparison with that of CdSe NCs.

4. Conclusions

In conclusion, we report on organometallic synthesis of CdTe/ZnSe semiconductor heterostructured nanocrystals, exhibiting a mixed type of carrier confinement. It is demonstrated that CdTe/ZnSe emission arises from the recombination of carriers within an interfacial layer, which is formed due to the cation/anion exchange in merging ZnSe and CdTe lattices. Fabricated nanocrystals show enhanced emission stability against etching and could be of potential use as florescence energy donors in FRET-based sensors, where an effective donor−acceptor distance is reduced due to interfacial localization of photogenerated carriers.

Acknowledgment. We gratefully acknowledge Bowling Green State University for financial support (SF07, RIC2008, RCE2008). This research made use of the facilities of the University of Michigan Electron Microbeam Analysis Laboratory and University of Toledo Instrumentation Center.

Supporting Information Available: Study of the aggregation-induced changes in the absorption profile of CdTe/ZnSe hetero-NCs is presented. This information is available free of charge via the Internet at http://pubs.acs.org.

References and Notes

(1) Peng, X. G.; Schlamp, M. C.; Kadavanich, A. V.; Alivisatos, A. P. *J. Am. Chem. Soc.* **1997**, *119*, 7019.
(2) Hines, M. A.; Guyot-Sionnest, P. *J. Phys. Chem.* **1996**, *100*, 468.
(3) Dabbousi, B. O.; RodriguezViejo, J.; Mikulec, F. V.; Heine, J. R.; Mattoussi, H.; Ober, R.; Jensen, K. F.; Bawendi, M. G. *J. Phys. Chem. B* **1997**, *101*, 9463.
(4) Zhao, J. L.; Zhang, J. Y.; Jiang, C. Y.; Bohnenberger, J.; Basche, T.; Mews, A. *J. Appl. Phys.* **2004**, *96*, 3206.
(5) Nizamoglu, S.; Ozel, T.; Sari, E.; Demir, H. V. *Nanotechnology.* **2007**, *18*, 065709.
(6) Steckel, J. S.; Snee, P.; Coe-Sullivan, S.; Zimmer, J. R.; Halpert, J. E.; Anikeeva, P.; Kim, L. A.; Bulovic, V.; Bawendi, M. G. *Angew Chem. Int. Ed.* **2006**, *45*, 5796.
(7) Bruchez, M.; Moronne, M.; Gin, P.; Weiss, S.; Alivisatos, A. P. *Science* **1998**, *281*, 2013.
(8) Mattoussi, H.; Mauro, J. M.; Goldman, E. R.; Anderson, G. P.; Sundar, V. C.; Mikulec, F. V.; Bawendi, M. G. *J. Am. Chem. Soc.* **2000**, *122*, 12142.
(9) Son, D. H.; Hughes, S. M.; Yin, Y. D.; Alivisatos, A. P. *Science* **2004**, *306*, 1009.
(10) Costa-Fernandez, J. M.; Pereiro, R.; Sanz-Medel, A. *Trends Anal. Chem.* **2006**, *25*, 207.
(11) Nirmal, M.; Dabbousi, B. O.; Bawendi, M. G.; Macklin, J. J.; Trautman, J. K.; Harris, T. D.; Brus, L. E. *Nature* **1996**, *383*, 802.
(12) Hohng, S.; Ha, T. *J. Am. Chem. Soc.* **2004**, *126*, 1324.
(13) Banin, U.; Bruchez, M.; Alivisatos, A. P.; Ha, T.; Weiss, S.; Chemla, D. S. *J. Chem. Phys.* **1999**, *110*, 1195.
(14) Li, Y. C.; Zhong, H. Z.; Li, R.; Zhou, Y.; Yang, C. H.; Li, Y. F. *Adv. Funct. Mater.* **2006**, *16*, 1705.
(15) Zhou, Y.; Li, Y. C.; Zhong, H. Z.; Hou, J. H.; Ding, Y. Q.; Yang, C. H.; Li, Y. F. *Nanotechnology* **2006**, *17*, 4041.
(16) Zhang, Y.; Wang, L. W.; Mascarenhas, A. *Nano Lett.* **2007**, *7*, 1264.
(17) Luque, A.; Marti, A.; Nozik, A. J. *MRS Bull.* **2007**, *32*, 236.
(18) Nemchinov, A.; Kirsanova, M.; Hewa-Kasakarage, N. N.; Zamkov, M. *J. Phys. Chem. C* **2008**, *112*, 9301.
(19) Doose, S. *Small* **2007**, *11*, 1856.
(20) Klimov, V. I.; Ivanov, S. A.; Nanda, J.; Achermann, M.; Bezel, I.; McGuire, J. A.; Piryatinski, A. *Nature* **2007**, *447*, 441.
(21) Chan, Y.; Steckel, J. S.; Snee, P. T.; Caruge, J. M.; Hodgkiss, J. M.; Nocera, D. G.; Bawendi, M. G. *Appl. Phys. Lett.* **2005**, *86*, 073102.
(22) Changa, J.; Takaia, T.; Godoa, K.; Makinoa, H.; Gotob, T.; Yaoa, T. *J. Cryst. Growth* **2003**, *251*, 612.
(23) Lee, J.Y.; Chang, J. H.; Yang, M.; Ahn, H. S.; Yi, S. N.; Goto, K.; Godo, K.; Makino, H.; Cho, M. W.; Yao, T.; Song, J. S. *Curr. Appl. Phys.* **2004**, *4*, 611.
(24) Willard, D. M.; Carillo, L. L.; Jung, J.; Van Orden, A. *Nano Lett.* **2001**, *1*, 469.
(25) (a) Medintz, I. L.; Clapp, A. R.; Mattoussi, H.; Goldman, E. R.; Fisher, B.; Mauro, J. M. *Nat. Mater.* **2003**, *2*, 630. (b) Medintz, I. L.; Clapp, A. R.; Melinger, J. S.; Deschamps, J. R.; Mattoussi, H. *Adv. Mater.* **2005**, *17*, 2450.
(26) Yu, W. W.; Wang, Y. A.; Peng, X. *Chem. Mater.* **2003**, *15*, 4300.
(27) Zhong, X. H.; Zhang, Z. H.; Liu, S. H.; Han, M. Y.; Knoll, W. *J. Phys. Chem. B* **2004**, *108*, 15552.
(28) Zhong, X. H.; Han, M. Y.; Dong, Z. L.; Dong, Z. L.; White, T. J.; Knoll, W. *J. Am. Chem. Soc.* **2003**, *125*, 8589.
(29) Bailey, R. E.; Nie, S. M. *J. Am. Chem. Soc.* **2003**, *125*, 7100.
(30) Yu, W. W.; Qu, L.; Guo, W.; Peng, X. *Chem. Mater.* **2003**, *15*, 2854.
(31) Battaglia, D.; Blackman, B.; Peng, X. G. *J. Am. Chem. Soc.* **2005**, *127*, 10889.
(32) El-Khoury, P. Z.; Tarnovsky, A. N. *Chem. Phys. Lett.* **2008**, *453*, 160.
(33) Singh, J. *Physics of Semiconductors and Their Heterostructures*; McGraw Hill, 1993.
(34) Dabbousi, B. O.; Rodriguez-Viejo, J.; Mikulec, F. V.; Heine, J. R.; Mattoussi, H.; Ober, R.; Jensen, K. F.; Bawendi, M. G. *J. Phys. Chem. B* **1997**, *101*, 9463.
(35) Klimov, V. I.; McBranch, D. W.; Leatherdale, C. A.; Bawendi, M. G. *Phys. Rev. B* **1999**, *60*, 13740.
(36) Klimov, V. I. *Annu. Rev. Phys. Chem.* **2007**, *58*, 635.
(37) Bernard, J. E.; Zunger, A. *Phys. Rev. B* **1987**, *36*, 3199.
(38) Fisher, B. R.; Eisler, H.-J.; Stott, N. E.; Bawendi, M. G. *J. Phys. Chem. B* **2004**, *108*, 143.

JP8106843